Evaluation of the Radiometric Performance of FY-3D MERSI-II Using Dome C, Antarctica

Zicheng Yin, Teng Li, Linlu Mei, Xiao Cheng, Lei Zheng, Qi Liang, and Xinqing Li

Abstract—**Continuous monitoring and assessment of satellite sensor radiometric response are crucial for timely detection of anomaly of the sensor performance, especially for operational optical sensors (e.g., FY-3D MERSI-II) beyond the expected lifespan. Improving calibration coefficients ensures the acquisition of high-precision and consistent observational Level 1 data records for long time-series researches. To evaluate the radiometric response stability of FY-3D MERSI-II in the reflective solar band, this study constructs parametric simplified and nonsimplified Warren bidirectional reflectance distribution function (BRDF) models using FY-3D MERSI-II nadir observation data at Dome C, Antarctica during the austral summer (October–February in next year) from 2019 to 2023. Subsequently, BRDF correction is applied to eliminate variations in the Dome C data caused by its non-Lambertian nature. The corrected data are analyzed for trends and compared with previous publications. The findings indicate that parameter simplification results in this study improve the calibration accuracy for band 3 (0.650 μm) and band 4 (0.865 μm) by 18.1% and 9.5%, respectively. Further analysis for the instrument degradation reveals that [the total multiyear degradation rate, average annual degradation rate] are within [$\pm 2.2\%$, $\pm 0.54\%$] and [$\pm 0.5\%$, $\pm 0.13\%$], respectively. Comparative validation results demonstrate good agreement with previous studies, showing a deviation of the average annual degradation rate between corresponding bands within $\pm 1\%$. It demonstrates that the stability of the MERSI-II is comparable to MODIS, which is one of the most frequently used medium-resolution sensors over last 25 years.**

Index Terms—**Bidirectional reflectance distribution function (BRDF), calibration, Dome C, FY-3D, medium resolution sensor.**

I. INTRODUCTION

FY-3D is the fourth satellite in China's second-generation polar-orbiting meteorological satellite series, launched on November 15, 2017, from the Taiyuan Satellite Launch Center [1]. FY-3D is equipped with ten remote sensing sensors, comprising four newly developed and six inherited and upgraded sensors, with the Moderate Resolution Spectral Imager II (MERSI-II) being one of the upgraded instruments. MERSI-II has 25 spectral channels covering the visible to mid-longwave infrared spectra, including six 250-m resolution channels (Band 1, Band 2, Band 3, Band 4, Band 24, and Band 25), which are mainly focused on the reflective solar band. In this study, we primarily use observation data in Band 3 and Band 4, which represent Red and NIR, respectively, (Fig. 1). And its rich spectral bands can be used for land surface temperature inversion [2], snow and ice monitoring [3], climate change research [4], and aerosol [5], fire detection product generation [6].

As satellites suffering from the impacts of harsh space and component aging during their in-orbit operation, the radiometric response performance of on-board sensors is inevitably subject to degrade. However, the current assessment of the radiometric response performance of FY-3D dominantly concentrates on prelaunch [7] or in-orbit periods [8], [9], [10] and lacks a long-term assessment of the radiometric response performance beyond its expected lifespan. As the core sensor of FY-3D, MERSI-II needs to meet the requirements for high-precision inversion of atmospheric, land, and oceanic parameters, which require consistent observation records over long time series. However, a prerequisite for acquiring high quality observations is the continuous monitoring and evaluation of the radiometric response performance of the satellite sensors. Therefore, in this study, we try to assess the stability of the radiometric response in the reflective solar band since the official operation of FY-3D MERSI-II.

The primary methods for monitoring and calibrating the radiometric response performance of sensors include prelaunch laboratory calibration [7], on-orbit on-board calibration [11], and on-orbit cross-calibration [12]. Given that many satellites lack conditions for on-board calibrations, the most commonly utilized alternative is on-orbit calibration based on vast and stable targets on Earth. Desert targets in Africa, South America, and Northwest China [10], [13], [14], [15], [16], as well as snow

Zicheng Yin is with the School of Geospatial Engineering and Science, Sun Yat-Sen University, Zhuhai 519082, China (e-mail: yinzch3@mail2.sysu.edu.cn).

Teng Li is with the School of Geospatial Engineering and Science, Southern Marine Science and Engineering Guangdong Laboratory, Sun Yat-Sen University, Zhuhai 519082, China (e-mail: liteng28@mail.sysu.edu.cn).

Linlu Mei is with the International Research Center of Big Data for Sustainable Development Goals, Beijing 100094, China, and also with Key Laboratory of Digital Earth Science, Aerospace Information Research Institute, Chinese Academy of Sciences, Beijing 100094, China (e-mail: mei@cbas.ac.cn).

Xiao Cheng is with the School of Geospatial Engineering and Science, Southern Marine Science and Engineering Guangdong Laboratory, Sun Yat-Sen University, Zhuhai 519000, China, and also with University Corporation for Polar Research (UCPR), Beijing 100875, China (e-mail: chengxiao9@mail.sysu.edu.cn).

Lei Zheng, Qi Liang, and Xinqing Li are with the School of Geospatial Engineering and Science, Southern Marine Science and Engineering Guangdong Laboratory, Sun Yat-Sen University, Zhuhai 519082, China (e-mail: zhenglei6@mail.sysu.edu.cn; liangq57@mail.sysu.edu.cn; lixinqing@sml-zhuhai.cn).

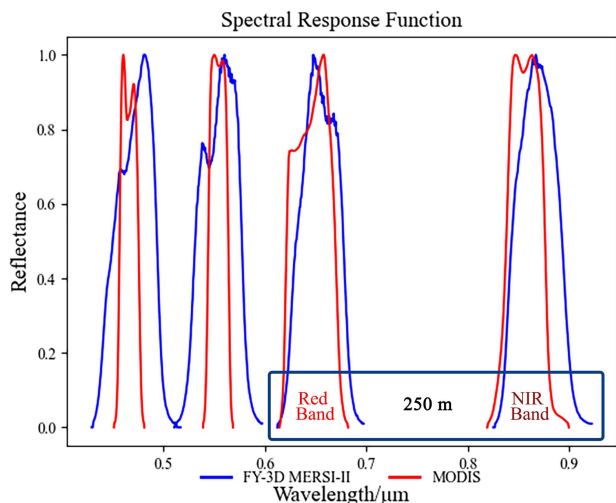Digital Object Identifier 10.1109/JSTARS.2024.3426968

Fig. 1.   Spectral response functions of FY-3D and MODIS in the reflective solar bands. The band 3 and band 4 data in box are used in this study.

and ice targets (Antarctic and Greenland) [16], [17], lake [18] and cloud (e.g., deep convective cloud, DCC) targets [14], [19], [20], [21] are widely used stable targets for remote sensing sensors calibrations globally. Compared to desert and DCC targets, ice and snow targets in polar regions exhibit superior spatial coherence and temporal stability. In addition, ice and snow targets perform better than desert and DCC targets in band those wavelengths less than 900 nm [22]. Among snow and ice targets, Cao et al. [23] demonstrated that Dome C in the Antarctic ice sheet is an excellent site for radiometric stability assessment. Many researchers have conducted radiometric stability studies of medium-resolution satellite sensors using Dome C. Xiong et al. [24] utilized Dome C to investigate the radiometric stability of MODIS in the reflective solar band and thermal infrared band, proving excellent long-term radiometric stability in these bands. Wang et al. [22] employed Dome C, along with two different sites in Antarctic and Greenland, to assess the radiometric stability of the FY-3 A MERSI over a long time series. They found a significant degradation in the blue band of the MERSI sensor. As shown in Fig. 1, MODIS and MERSI-II sensors have similar band settings. Especially, as the follower, MERSI-II's spectral response functions and spatial resolution settings in the red and near-infrared bands resemble closely to those of MODIS. It is noteworthy that the FY-3 A MERSI, serving as the predecessor to MERSI-II, shares these characteristics and both sensors have successful radiometric stability evaluations at Dome C [22]. The success of MODIS and MERSI demonstrates the feasibility of conducting the radiometric stability assessment of the MERSI-II sensor at Dome C. The surface of Dome C is snow, which is a very anisotropic feature, so normally we need to use the bidirectional reflectance distribution function (BRDF) model to correct the angle [25], [26]. Many of the aforementioned studies utilized the BRDF model proposed by Warren [27], with variations in the use of either the parameter-simplified version [23] or the original version [24]. The impact of parameter simplification on the calibration effectiveness of the model remains an unexplored area.

In order to investigate the potential impact of the overdue service of FY-3D on the radiometric stability of MERSI-II, we identified two target areas at Dome C, which is widely recognized as a calibration site, to investigate and assess the long-term radiometric response performance of FY-3D MERSI-II. Relevant observational data for the austral summer over the five-year period from 2019 to 2023 were collected for these two areas. Using the observation data, two BRDF models, both parametric nonsimplified and simplified, were established. These models were applied for BRDF correction of the observational data to diminish non-Lambertian variations from ice and snow targets. Subsequently, the study employed quadratic fitting on the BRDF-corrected data to characterize the long-term trend of radiometric response performance. Based on this, the radiometric degradation rate of relevant spectral bands were calculated. Using radiometric degradation rate as a metric indicator, the study conducted a long-term assessment of the radiometric response stability of FY-3D MERSI-II in the reflective solar band. Comparative analysis and validation against results from other similar medium-resolution sensor studies were also conducted. Building upon this, the study delved into the analysis of trends and reasons for the seasonal and perennial variations in top-of-atmosphere (TOA) reflectance for the target areas, as well as the impact of model simplification on the correction effectiveness of the models.

II. SITE DESCRIPTION AND DATA SELECTION

A. Introduction to Target Area

Dome C is located in the southeastern part of the Antarctic ice sheet (75.1°S, 123.4°E). With an elevation of approximately 3233 m. Dome C has a gentle slope, low snow accumulation, and is considered one of the most uniform land surface on Earth. At typical spatial scales relevant to common satellite sensor resolutions, both reflectance and temperature exhibit remarkable uniformity [28], [29]. Atmospheric conditions of Dome C are exceptionally cold, dry, and thin, with consistently low cloud coverage. Its remote location deep in land(>1000 km from the coast) results in lower aerosol and water vapor content in the atmosphere, contributing to reduced atmospheric uncertainties [30], [31].

Due to these unique surface and atmospheric characteristics, Dome C holds a pivotal position in the field of sensor calibration and validation [29], [32]. Numerous applications have been successfully conducted at Dome C for the calibration of sensors without onboard spaceborne calibrators [33], as well as the validation of sensors equipped with spaceborne calibrators [22], [23], [24]. This applies to various spectral bands, including visible and near-infrared [16], [33], thermal infrared [34], microwave [12], and even nighttime band data [35], [36].

The Paul-Émile Victor Institute (IPEV) of France and the National Antarctic Research Program (PNRA) of Italy jointly established and operate a permanent research station, Concordia Station, in the Dome C. This station conducts routine ground measurements of atmospheric parameters and serves as a base for on-site activities related to satellite remote sensing calibration and validation. In addition, another research station
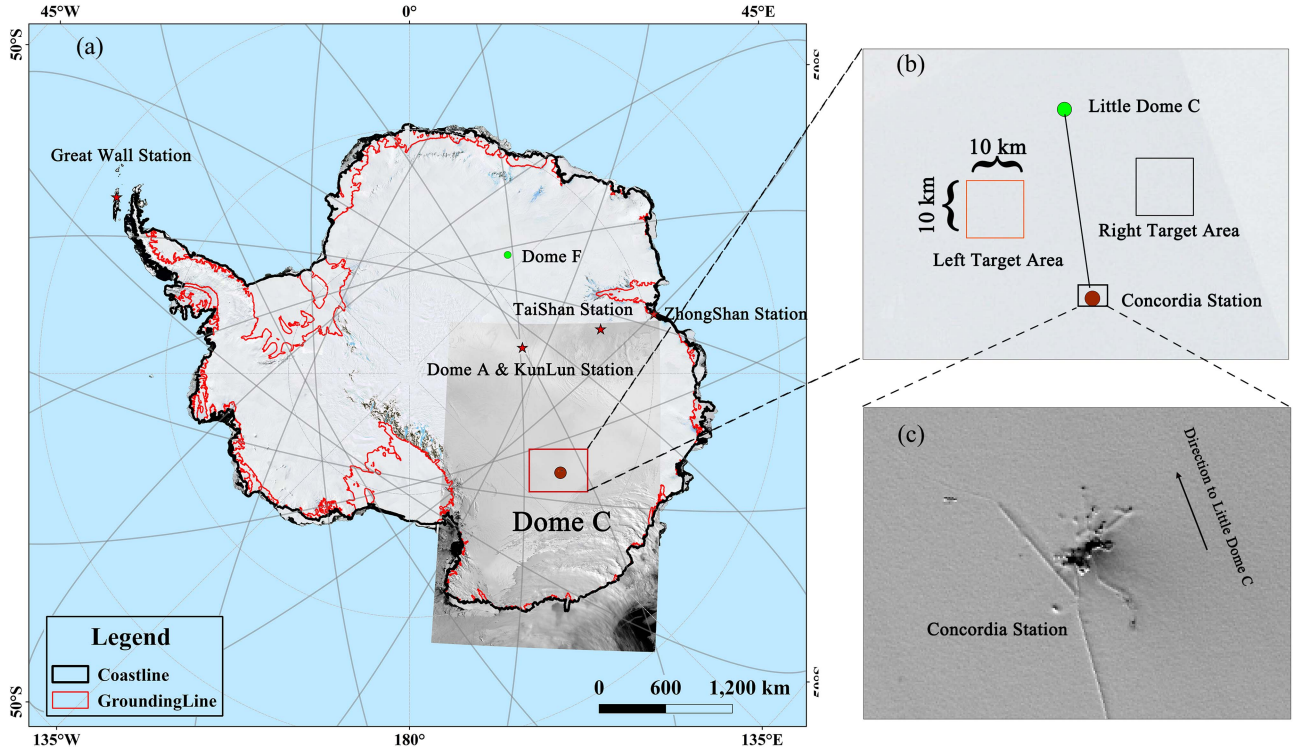
Fig. 2. (a) Location of Dome C on the Antarctic (Overlaid by a scene of MERSI-II level-1 imagery). The solid grey line is the FY-3D satellite orbit. (b) Distribution of target areas in the Dome C region. (c) Concordia Station on Landsat 8 panchromatic image with 15-m resolution, with an arrow indicating the direction of Little Dome C.

named Little Dome C located 30 km from Concordia Station, where researchers engage in deep ice core drilling activities. Human activities footprints, such as those depicted in Fig. 2(c) showing tracks left by vehicle transport, are evident between Little Dome C and Concordia Station. To mitigate potential impacts on the homogeneity of the land surface and subsequent experiments, this study selected target areas on both sides of the line connecting the two stations, each measuring 10 km in length and width, for further experimentation. Details of the target areas are illustrated in Fig. 2(b).

B. Data Selection

Due to the high latitude of Dome C (75.1°S) and the fact that FY-3D is a polar-orbiting satellite, as depicted by the solid gray line in Fig. 2(c), FY-3D typically revisits Dome C multiple times within one day. In addition, approximately every 4–6 d, there is a nadir view pass over Dome C (defined in this study as within a range of ±50 km from the nadir orbit at Dome C). To keep the consistency of observational geometry, this study specifically focuses on these near nadir data. Restricting the data to near-nadir observations minimizes any impact due to varying scan mirror angle of incidence (AOI) [24]. In terms of time, this study selects data during austral summer, which spans from October 15th each year to February 28th the next year. The study spans a total of five years of data from 2019 to 2023 (FY-3D data distribution began on January 1st, 2019, resulting in the absence of the first half of the 2018 to 2019 austral summer). Regarding spectral bands, this study focuses on the red (band 3, ~650 nm)

and near-infrared (band 4, ~865 nm) in the reflective solar bands. Finally, we obtained the TOA reflectance, solar zenith angle, solar azimuth angle, sensor zenith angle, and sensor azimuth angle in the left and right target regions, as shown in Fig. 2(b).

III. METHODOLOGY

A. Radiometric Calibration and Geometric Correction

First, we conduct radiometric calibration on the raw reflectance data from January 2019 to February 2023. The radiometric calibration transforms the raw reflectance data to TOA reflectance using the inherent calibration coefficients. The radiometric calibration equation is provided as follows:

$$\rho_{\text{TOA},i} = (\alpha_i \cdot V_{\text{DN}i} + \beta_i) \cdot \frac{d^2}{\cos \theta_s} \qquad (1)$$

where α_i and β_i are the calibration slopes and intercepts of the ith band of MERSI-II, V_{DN_i} is the digital number of the ith band of MERSI-II, d is the solar-Earth distance index, and θ_s is the solar zenith angle.

Subsequently, the TOA reflectance data were geometrically mapped using the geographic lookup table method. In the geometric correction process, due to the mismatch in resolution between the band data and the geolocation array, it is necessary to resample the geolocation array to four times the original resolution. Before resampling, we converted the latitude and longitude data to into Antarctic Polar Stereographic projection (EPSG: 3031) values.

B. Cloud Contamination Removal and Homogeneity Analysis

Although the Dome C is cloud-free for about 70% of the year, the data selected for this study inevitably face contamination from clouds. Therefore, it is imperative to perform cloud contamination removal on the TOA reflectance data. Due to the low contrast in reflection between the snow and cloud, both of which have high reflectance, cloud contamination removal at Dome C is not easy. Spatial nonuniformity analysis is an effective method for cloud contamination removal. Previous studies have utilized various bands, with visible and near-infrared bands being the most prevalent [23], [33], [37]. In line with these precedent, we adopt a similar approach, utilizing the red band (band 3, 0.650 μm) and the near-infrared band (band 4, 0.865 μm) data for the subsequent steps of cloud contamination removal. First, the mean and the standard deviation of the TOA reflectance in target areas are calculated, and if the ratio of the standard deviation to the mean is greater than 0.1, the data are empirically considered contaminated by clouds which will be directly discarded. Finally, pixels whose TOA reflectance differs from the mean by more than 5% of the standard deviation were eliminated (The setting of these thresholds was also obtained from previous studies.). Afterward we did a visual check to make sure that no large cloud or cloud shadow pixels were left in the following analyses.

After removing the cloud contamination from the TOA reflectance data, in order to verify the effectiveness of the cloud contamination removal and the spatial homogeneity at Dome C, the homogeneity index N of the TOA reflectance data in the target area was calculated. We use the following equation by replacing the four bands in the original equation with the two bands in this study with reference to the setup of Loeb [38]. The equation we used is provided as follows:

$$N = \frac{1}{2}\left(\frac{\sigma_3}{R_3} + \frac{\sigma_4}{R_4}\right) \times 100\% \qquad (2)$$

where σ_3 and σ_4 denote the standard deviations of TOA reflectance for bands 3 and 4 within the target areas, and R_3 and R_4 represent the means of TOA reflectance for bands 3 and 4 within the target areas.

C. Snow and Ice Target BRDF Effect Correction

The raw TOA reflectance data are affected by the BRDF effect and cannot be directly used for radiometric stability assessment, so in this study, the Warren BRDF model [27] is established by fitting the parameters from the available data after cloud removal. The solar zenith angle, sensor zenith angle, and relative azimuth angle used in this and subsequent steps are all averaged over the 10 × 10-km subset. The equation for the BRDF model is as follows:

$$\rho(\theta, \psi, \varphi) = c_1 + c_2 \cos(\pi - \varphi) + c_3 \cos[2(\pi - \varphi)]$$
$$c_1 = a_0 + a_1[1 - \cos(\psi)]$$
$$c_2 = a_2[1 - \cos(\psi)]$$
$$c_3 = a_3[1 - \cos(\psi)]$$

$$a_i = b_{0i} + b_{1i}\cos(\theta) + b_{2i}\cos^2(\theta) \quad (i = 0, 1, 2) \quad (3)$$

where θ is the solar zenith angle, ψ is the sensor zenith angle, and φ is the relative azimuth angle.

It should be noted that Warren's BRDF model for snow and ice is based on ground situ measurements, while satellite measurements have the additional influence of the atmosphere. Based on the stable atmospheric conditions at Dome C [30], and because of the higher elevation, the atmospheric impact is further reduced [39], we follow Cao et al. [23]'s assumption which ignores the influence of the atmosphere on the satellite observations and directly use the TOA reflectance to represent the surface reflectance. Please note all the subsequent studies are carried out based on such premise.

Since this study uses near-nadir observations, the original BRDF model can be simplified. The sensor zenith angle and relative azimuth angle are made to be 0, and the simplified BRDF model equation is as follows:

$$\rho(\theta, \psi, \varphi) = b_{00} + b_{10}\cos(\theta) + b_{20}\cos^2(\theta). \qquad (4)$$

Following the construction of both the original and parameter-simplified BRDF models using the same data, these models were utilized to generate model-predicted TOA reflectance. Subsequently, the model-predicted TOA reflectance was employed to normalize the original TOA reflectance, effectively eliminating the BRDF effect. The normalization was achieved using the following equation:

$$R_{\text{norm}} = \rho_{\text{TOA}} / \rho_{\text{modeled}} \qquad (5)$$

where R_{norm} represents the normalized TOA reflectance, ρ_{TOA} represents the raw TOA reflectance, and ρ_{modeled} represents the model-predicted TOA reflectance.

In addition, we compared the residuals of the two models to verify the influence of parameter simplification on the effectiveness of BRDF correction of the models.

D. Calculation of Radiometric Degradation

A quadratic polynomial fit is applied to the normalized reflectance R_{norm} after removal of the BRDF effect to establish an equation between R_{norm} and time t, which can be expressed as

$$R_{\text{norm}} = a_0 + a_1 t + a_2 t^2. \qquad (6)$$

By calculating the radiometric degradation in each band, we evaluate the radiometric stability of the FY-3D satellite data over the Antarctic. The equation for calculating the radiometric degradation is as follows:

$$D_{\text{total}} = \frac{\hat{R}_{\text{TOA}}(t_2) - \hat{R}_{\text{TOA}}(t_1)}{\hat{R}_{\text{TOA}}(t_1)} \times 100\%$$

$$D_{\text{annual}} = \frac{D_{\text{total}}}{t_2 - t_1} \times 365 \times 100\% \qquad (7)$$

where D_{total} represents the total radiometric degradation during the time intervals t_1 and t_2, and D_{annual} represents the annual average radiometric degradation during the time intervals t_1 and t_2.
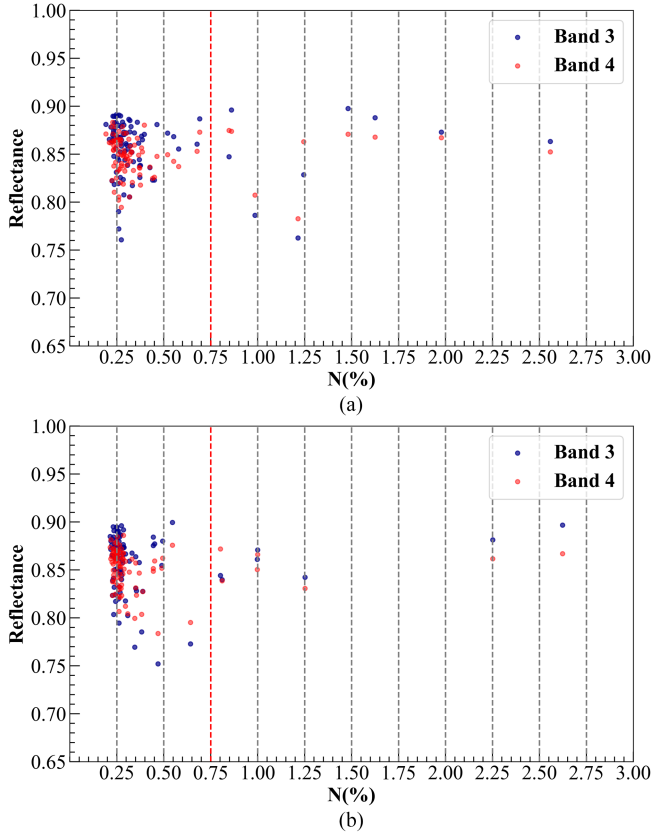
Fig. 3. Homogeneity index N of TOA Reflectance in (a) left and (b) right target areas.

IV. RESULT

A. Homogeneity Index for TOA Reflectance

After applying (2) to calculate the homogeneity index N for all target area data, we illustrate the relation between N and the TOA reflectance of band 3 and band 4, as illustrated in Fig. 3. In general, a lower N value indicates better homogeneity of TOA reflectance in the target area. Previous research suggests that a threshold of $N = 0.75\%$ is critical for assessing homogeneity [38]. Fig. 3 demonstrates that approximately 94.4% of observations in the left target area and 93.3% in the right target area have N values below 0.75%. This implies that the majority of observations effectively represent a cloud-free and homogeneous ice surface after the initial cloud contamination removal step. This outcome meet the requirements for subsequent applications and analyses.

B. Analysis of the Trend in TOA Reflectance With Solar Illumination

Fig. 4(a) and (b) illustrate the time series of TOA reflectance for band 3 and band 4 in the left and right target areas. Following radiometric calibration, the TOA reflectance for band 3 range from 0.75 to 0.90, while those for band 4 range from 0.78 to 0.89 over the five-year observation period. Notably, there is minimal disparity in TOA reflectance for both band 3 and band 4 between the left and right target areas at the same time, indicating a high degree of homogeneity across a large area of
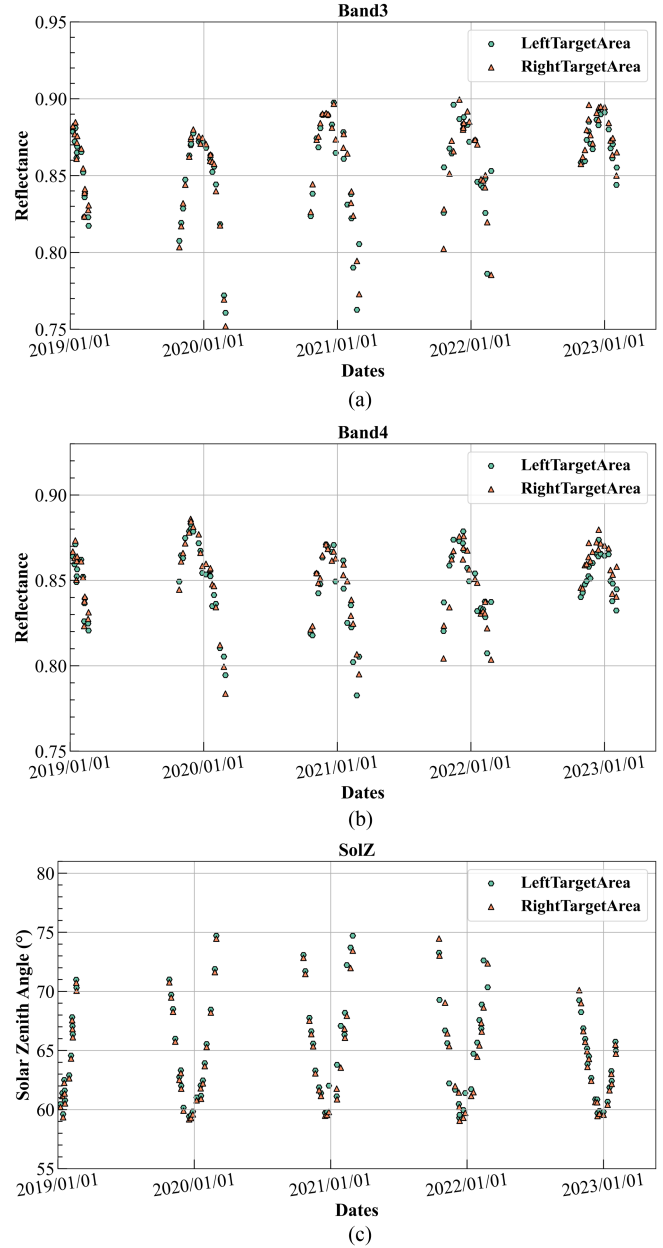

Fig. 4. Time series of (a) band 3, (b) band 4 raw TOA reflectance, and (c) solar zenith angle in the left and right target areas.

Dome C. Examining the seasonal trends, both band 3 and band 4 exhibit similar patterns. They start to rise in October each year, reach their peak in December, and then begin to decline. The overall trend is roughly symmetrical, with December acting as the central axis. If the surface reflectance properties at Dome C were Lambertian, the trend would be a relatively stable horizontal line. However, the observed trend during each summer resembles a parabola, closely correlated with the variations in solar zenith angle depicted in Fig. 4(c). This is attributed to the influence of the BRDF effect, where the non-Lambertian nature of Dome C snow surface leads to correlated variations in TOA reflectance. To substantiate this claim, we conducted the following investigation.
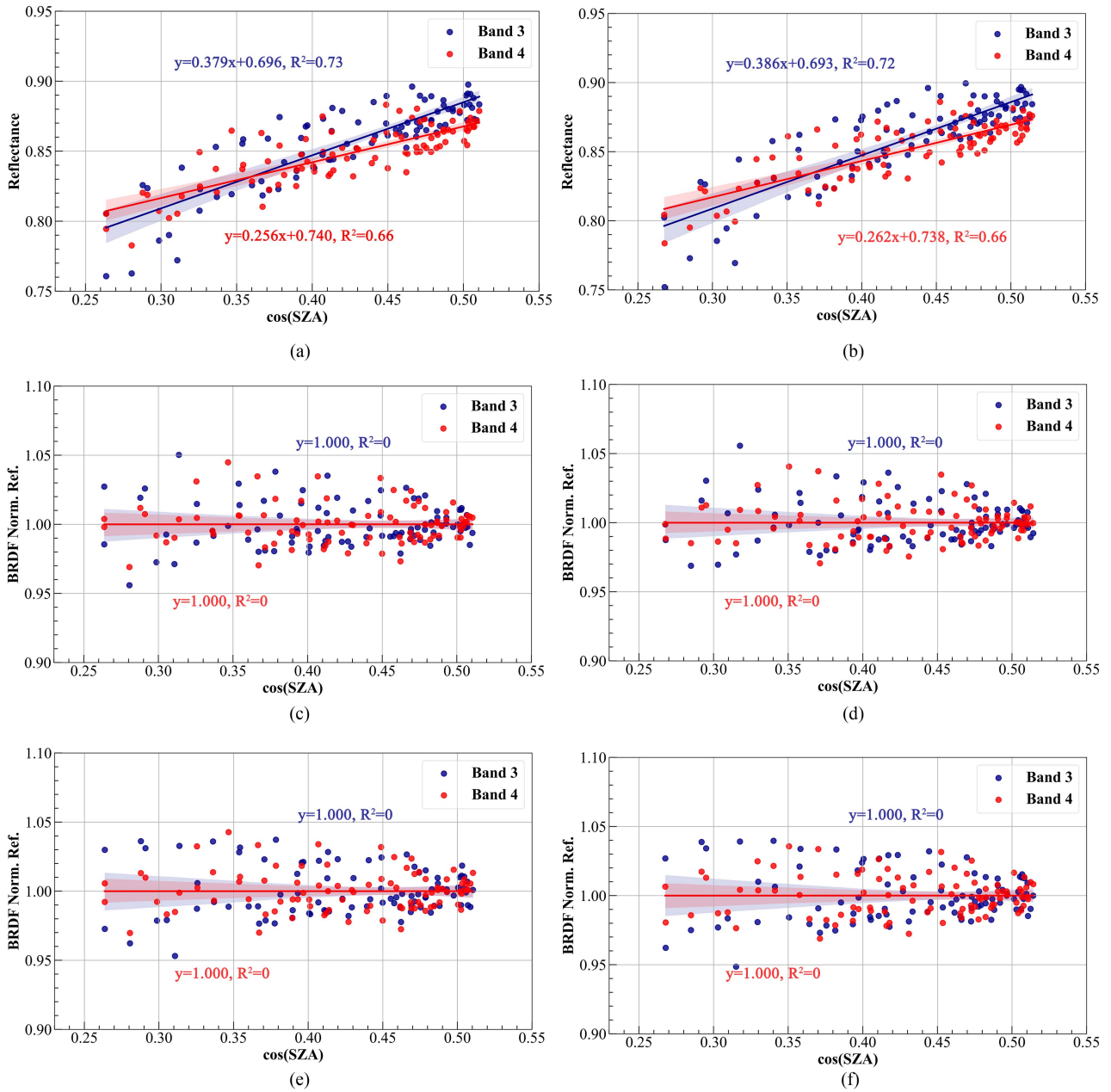
Fig. 5.   Correlation between raw TOA reflectance and cosine of solar zenith angle in the (a) left and (b) right target areas; the correlation between normolized TOA reflectance after original model BRDF correction and cosine of solar zenith angle in the (c) left and (d) right target areas; the correlation between normolized TOA reflectance after simplified model BRDF correction and cosine of solar zenith angle in the (e) left and (f) right target areas.

Previous studies indicated that solar zenith angle is a major factor influencing the BRDF characteristics of snow and ice target [40], [41]. Fig. 4(c) presents the variation in solar zenith angle for observations near nadir at Dome C: decreasing from October to reaching a minimum in December, followed by an ascent. The variation pattern of solar zenith and the TOA reflectance are comparable in time yet opposite in direction, which proves that the main factor influencing the trend of near-nadir raw TOA reflectance in band 3 and band 4 is the anisotropic nature of snow and ice targets [42]. To further substantiate this perspective, we explored the correlation between raw TOA reflectance and cosine of solar zenith angle in the left and

right target areas, as shown in Fig. 5(a) and (b). The results indicate that in all cases, reflectance steadily increases with an decrease in cosine of solar zenith angle with significance. Fig. 5(c)–(f) reveal the correlation between BRDF-corrected TOA reflectance and cosine of solar zenith angle. It is evident that after BRDF correction, the correlation between TOA reflectance and cosine of solar zenith angle is nearly zero. The fitted curves indicate a trend almost identical to a line nearly keep constant value of 1, suggesting that the non-Lambertian variations in raw TOA reflectance due to the anisotropic nature of snow and ice targets are effectively diminished after BRDF correction.
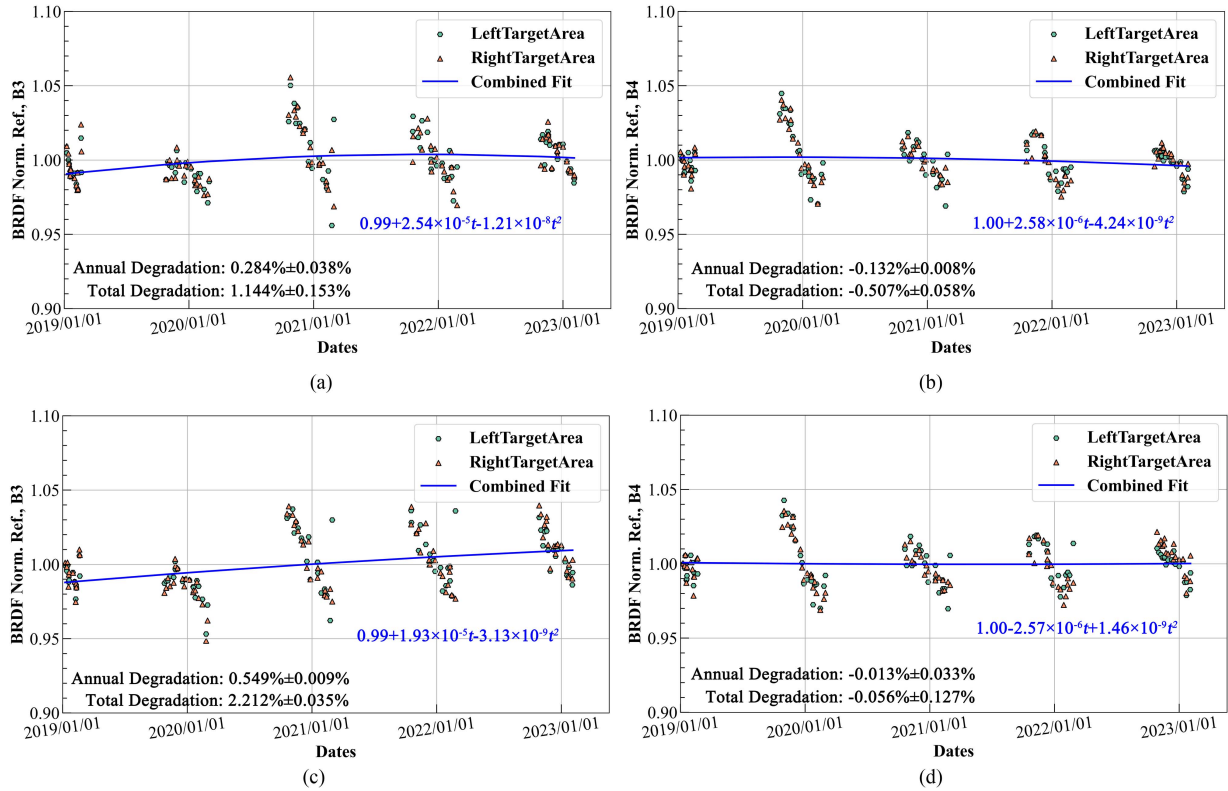
Fig. 6. Time series of (a) band 3, (b) band 4 normalized TOA reflectance R_{norm} after normalization using the original Warren BRDF model; time series of (c) band 3, and (d) band 4 normalized TOA reflectance R_{norm} after normalization using the simplified Warren BRDF model.

C. Result of Radiometric Degradation

Using observation data from January 2019 to February 2023, we performed parameter fitting for the original and simplified BRDF model equations [(3) and (4)] to establish two different BRDF models. The specific parameters of these models are detailed in Table II. In addition, the table includes residuals for the model before and after parameter simplification. The residuals for the red and near-infrared bands before simplification are 1.235% and 1.053%, respectively, while the simplified model yields values of 1.458% and 1.153%. This suggests that parameter simplification negatively impacts the BRDF correction effect, resulting in an 18.1% and 9.5% increase in residuals for band 3 and band 4, respectively.

Fig. 6 illustrates the time series of R_{norm} along with the final degradation rate calculation results. Since there is almost no difference in the normalized TOA reflectance between the left and right target areas, the decision is made to merge the two sides during the data processing for time series fitting. The blue curves with their corresponding equation in the figure depict the relationship function between R_{norm} and time t obtained through (6). In theory, if the radiometric response characteristics of MERSI-II bands remain constant, R_{norm} should be a constant value. However, as shown in Fig. 6, R_{norm} changes over time, indicating temporal variations in the radiometric response characteristics of MERSI-II bands. Regarding the overall trend, FY-3D MERSI-II remains stable in both red and near-infrared bands. The constants are close to or equal to 1 in the time-series fitting formulas of

both the original and simplified BRDF models, with coefficients for subsequent primary and secondary terms close to 0. This suggests that R_{norm} undergoes very small deviation above and below one over time. Finally, (7) is utilized to calculate specific radiometric degradation for the quantification of the radiometric stability of FY-3D MERSI-II reflective solar bands. Results indicate that the near-infrared bands exhibit relatively better stability, with a total multiyear degradation rate for red bands within ±2.2% and an average annual degradation rate within ±0.54%. On the other hand, the total multiyear degradation rate for near-infrared bands is within ±0.5%, and the average annual degradation rate is within ±0.5%. The near-infrared band shows a multiyear total degradation rate of ±0.5% with an average annual degradation rate of ±0.13% or less. The values after ± in the figure represent the uncertainty of the radiometric degradation, which is obtained by calculating the difference between the radiometric degradation of the left and right target area.

V. DISCUSSION

A. Evaluation of the Results of the Radiometric Stability Assessment

Medium-resolution optical remote sensing has decades of history in Earth observation, and in recent years, significant progress has been made by researchers in assessing the radiometric performance of those medium-resolution sensors [20], [22], [41], [43], [44], [45]. In order to validate our assessment

TABLE I
PARAMETERS AND RESIDUALS OF THE ORIGINAL AND SIMPLIFIED MODELS

		$i=0$	$i=1$	$i=2$	$i=3$	Residuals(%)
Band3	Original Model	$b_{00} = 0.361$ $b_{10} = 1.959$ $b_{20} = -1.872$	$b_{01} = 431.580$ $b_{11} = -2131.330$ $b_{21} = 2598.653$	$b_{02} = 576.838$ $b_{12} = -2850.522$ $b_{22} = 3477.096$	$b_{03} = 145.445$ $b_{13} = -720.064$ $b_{23} = 879.461$	1.235
	Simplified Model	$b_{00} = 0.537$ $b_{10} = 1.241$ $b_{20} = -1.053$	/	/	/	1.458
Band4	Original Model	$b_{00} = 0.583$ $b_{10} = 1.027$ $b_{20} = -0.941$	$b_{01} = 379.072$ $b_{11} = -1758.078$ $b_{21} = 2025.993$	$b_{02} = 506.736$ $b_{12} = -2350.484$ $b_{22} = 2707.501$	$b_{03} = 127.731$ $b_{13} = -592.722$ $b_{23} = 682.885$	1.053
	Simplified Model	$b_{00} = 0.650$ $b_{10} = 0.711$ $b_{20} = -0.559$	/	/	/	1.153

TABLE II
ANNUAL DEGARDATION OF MEDIUM-RESOLUTION SATELLITE SENSORS

Sensor	Target Area	Red band	Near-infrared band	Author
MERSI-II	**Snow**	**±0.54%**	**±0.13%**	**This Study**
	DCC	±0.03%	±0.44%	Zhang et al.[20]
MERSI-I	Snow	±0.33%	±0.74%	Wang et al.[22]
	DCC	±0.61%	±0.13%	Chen et al.[43]
	Desert	±0.21%	±0.54%	Sun et al.[44]
MODIS	Snow	0.17%-0.25%	1.0%	Wu et al.[41]
	DCC	1%	1.0%	Bhatt et al.[45]

results, we compared our assessment results with previous studies (Table I). In the previous studies in Table I, in the red band, the mean value is ±0.178% with a standard deviation of ±0.422%, and in the near-infrared band, the mean value is ±0.642% with a standard deviation of ±0.34%. The results of this study are within two standard deviations of the error in both bands, with a 95% confidence level. It is evident that the results from this study are highly consistent with those obtained from other medium-resolution satellite sensors, particularly exhibiting close resemblance to the results obtained from the MERSI sensor based on DCC targets [43]. This consistency enhances the credibility of the results obtained in this study. Furthermore, among the previous studies, the most informative one is Zhang et al. [20]'s study, in which the same data were used as this study and the time span of the data mostly overlaps (January 2018 to January 2023 for Zhang et al. [20]'s study and January 2019 to January 2023 for this study). However, due to the different target of the study, it produces a discrepancy in the results, which is in the normal range of the differences, and all of them can be considered as the results with informative value. On the other

hand, in the near-infrared band, it is not difficult to find that FY series satellite have lower radiometric degradation than MODIS. This is mainly due to the fact that MODIS has been in operation for more than 25 years, and the instrumentation has already deteriorated to a considerable degree.

Up to this point, there has not been a comparable study utilizing alternative methods to assess the radiometric stability of FY-3D MERSI-II. Therefore, for the purpose of comparing and evaluating results, similar assessments from other medium-resolution satellite sensors were employed. However, it is essential to acknowledge the significant differences in the construction of various sensors, which might impact the validation results. Consequently, our future research goal is to develop more methods specific to FY-3D MERSI-II, yielding additional results for cross-validation. In addition, we are considering broadening the wavelength bands used in my study, especially those, such as blue band, which have previously been shown to be heavily degraded in other studies [20], [22].

B. Analysis of the BRDF Correction Effects of the Model

This study calculated the residuals of the model before and after parameter simplification (Based on which sensor zenith angle and relative azimuth angle are made to be zero). The residuals for the red and near-infrared bands in the original model were 1.24% and 1.06%, respectively, while the corresponding values after simplification were 1.42% and 1.13%. These results indicate that parameter simplification has a negative impact on the BRDF correction effect. The reason behind this lies in the fact that the simplified model only considers the influence of solar zenith angle on the BRDF effect. However, in reality, both the sensor zenith angle and the relative azimuth angle also have similar effects with solar geometry. Although the data we use are near-nadir, as depicted in Fig. 7, the sensor zenith angle is not precisely 0, and certain value even exceeds 15° in extreme cases.

The methodology used in this study involves the BRDF model, where we obtained the parameters of the BRDF model using TOA reflectance data through a linear fit. In this type of
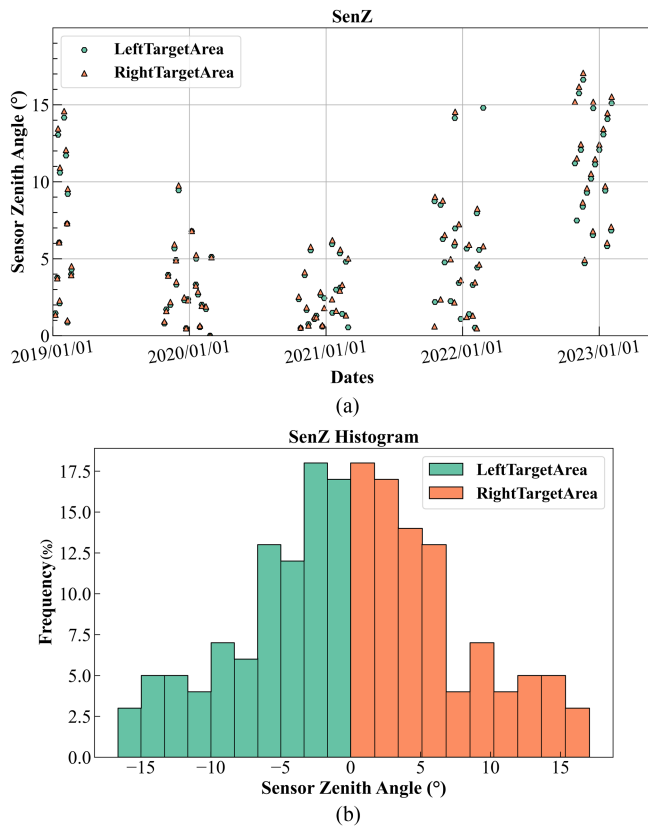
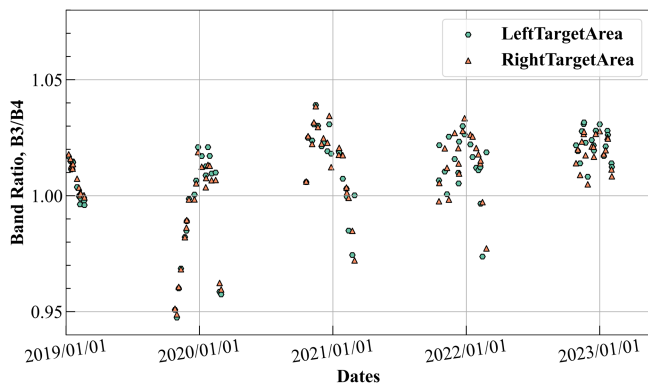Fig. 7. (a) Time series and (b) histogram of sensor zenith angles.

Fig. 8. Time series of band ratio.

fitting, small variations in TOA reflectance may be smoothed or masked. Therefore, a more sensitive method is required to detect any subtle changes in TOA reflectance. One such method is the analysis of the band ratio (band 3/band 4) to monitor relative changes [23]. This ratio is highly sensitive to small changes and can reveal differences in the BRDF between two bands. If the BRDF of band 3 and band 4 were identical, the band ratio should be a constant value. However, as shown in Fig. 8, the band ratio exhibits a range of nearly 10% over the five-year period. This indicates that the BRDF of band 3 and band 4 are not identical. The discrepancy is mainly due to the fact that the data used in this study is TOA reflectance, not surface reflectance.

TOA reflectance is influenced by wavelength-dependent atmospheric Rayleigh scattering and ozone effects [23]. With an increase in solar zenith angle and atmospheric path length, short-wavelength Rayleigh scattering and ozone absorption become more prominent compared to longer wavelengths, leading to changes in the band ratio. In this study, we treat the anisotropic nature of snow and ice targets and atmospheric effects in the same model, which results in separate BRDF for each band.

VI. CONCLUSION

In this study, we normalized the raw TOA reflectance by two versions of Warren's BRDF model, diminished the change information related to the BRDF characteristics of the snow and ice targets, and obtained the parameter reflecting the changes in the radiometric performance of the remote sensors. Finally, based on the data in both sides target areas, the trend analysis reveals revealing the radiometric response degradation of FY-3D MERSI-II from January 2019 to the end of February 2023. The residuals of the two different models were compared, and the results were contrasted with related studies on other medium-resolution satellite sensors. The conclusions drawn are as follows.

1) Parameter simplification has a negative impact on the model BRDF correction effect. The residuals for the red and near-infrared bands in the original model were 1.235% and 1.053%, respectively, while the corresponding values after simplification were 1.458% and 1.153%. The simplified model based on the near-nadir assumption may result in an approximate 10–20% increase in residual.
2) In terms of radiometric stability, the red and near-infrared bands of FY-3D MERSI-II exhibit relative stability. The total multiyear degradation rate for the red band is within $\pm2.2\%$, with an average annual degradation rate within $\pm0.54\%$. For the near-infrared band, the total multiyear degradation rate is within $\pm0.5\%$, with an average annual degradation rate within $\pm0.13\%$. This outcome is highly consistent with related research on other medium-resolution satellite sensors, indicating a high level of credibility.

In summary, this study elucidates the impact of FY-3D exceeding its expected service life on the radiometric stability of MERSI-II in the solar reflective bands. It fills a gap in the lack of long-term assessment of the radiometric response performance of FY-3D, while also comparing the influence of parameter simplification in Warren's BRDF modeling results. However, the study currently uses TOA reflectance instead of surface reflectance, and addressing the atmospheric impact on the research will be a focus of future work.

REFERENCES

[1] H. Wang et al., "A split window algorithm for retrieving land surface temperature from FY-3D MERSI-2 data," *Remote Sens.*, vol. 11, no. 18, pp. 2083–2107, 2019.
[2] K. Tang, H. Zhu, P. Ni, R. Li, and C. Fan, "Retrieving land surface temperature from chinese FY-3D MERSI-2 data using an operational split window algorithm," *IEEE J. Sel. Topics Appl. Earth Observ. Remote Sens.*, vol. 14, pp. 6639–6651, 2021.

[3] X. Zheng, F. Hui, Z. Huang, T. Wang, H. Huang, and Q. Wang, "Ice/snow surface temperature retrieval from chinese FY-3D MERSI-II data: Algorithm and preliminary validation," *IEEE Trans. Geosci. Remote Sens.*, vol. 60, 2022, Art. no. 4512715.

[4] Y. Si et al., "A novel algorithm of haze identification based on FY3D/MERSI-II remote sensing data," *Remote Sens.*, vol. 15, no. 2, pp. 438–457, 2023.

[5] Q. Wang, S. Li, J. Yang, D. Zhou, and G. Song, "A high-precision aerosol retrieval algorithm for FY-3D MERSI-II images," *Environ. Int.*, vol. 173, 2023, Art. no. 107841.

[6] J. Chen et al., "The Fengyun-3D (FY-3D) global active fire product: Principle, methodology and validation," *Earth System Sci. Data*, vol. 14, no. 8, pp. 3489–3508, 2022.

[7] N. Xu et al., "Prelaunch calibration and radiometric performance of the advanced MERSI II on FengYun-3D," *IEEE Trans. Geosci. Remote Sens.*, vol. 56, no. 8, pp. 4866–4875, Aug. 2018.

[8] X. Hu et al., "Preliminary selection and characterization of pseudo-invariant calibration sites in northwest China," *Remote Sens.*, vol. 12, no. 16, pp. 2517–2542, 2020.

[9] R. Wu et al., "FY-3D MERSI on-orbit radiometric calibration from the lunar view," *Sensors*, vol. 20, no. 17, pp. 4690–4702, 2020.

[10] J. Han, Z. Tao, Y. Xie, H. Li, H. Yi, and X. Guan, "Validation of the TOA products of the Baotou sandy site with Landsat8/OLI considering BRDF correction," *IEEE Trans. Geosci. Remote Sens.*, vol. 61, 2023, Art. no. 5401611.

[11] X. Hu et al., "Calibration for the solar reflective bands of medium resolution spectral imager onboard FY-3A," *IEEE Trans. Geosci. Remote Sens.*, vol. 50, no. 12, pp. 4915–4928, Dec. 2012.

[12] S. Wu and J. Chen, "Instrument performance and cross calibration of FY-3C MWRI," in *Proc. IEEE Int. Geosci. Remote Sens. Symp.*, 2016, pp. 388–391.

[13] J. Han, Z. Tao, Y. Xie, H. Li, Q. Liu, and X. Guan, "A novel radiometric cross-calibration of GF-6/WFV with MODIS at the Dunhuang radiometric calibration site," *IEEE J. Sel. Topics Appl. Earth Observ. Remote Sens.*, vol. 14, pp. 1645–1653, 2021.

[14] R. Bhatt et al., "Initial stability assessment of S-NPP VIIRS reflective solar band calibration using invariant desert and deep convective cloud targets," *Remote Sens.*, vol. 6, no. 4, pp. 2809–2826, 2014.

[15] X. Hu et al., "Characterization of CRCS dunhuang test site and vicarious calibration utilization for Fengyun (FY) series sensors," *Can. J. Remote Sens.*, vol. 36, no. 5, pp. 566–582, 2010.

[16] S. Uprety and C. Cao, "Radiometric and spectral characterization and comparison of the antarctic Dome C. and Sonoran desert sites for the calibration and validation of visible and near-infrared radiometers," *J. Appl. Remote Sens.*, vol. 6, no. 1, pp. 063541–063541, 2012.

[17] S. Masonis and S. Warren, "Gain of the AVHRR visible channel as tracked using bidirectional reflectance of antarctic and Greenland snow," *Int. J. Remote Sens.*, vol. 22, no. 8, pp. 1495–1520, 2001.

[18] L. Yan et al., "Radiometric calibration of Fengyun-3D MERSI-II satellite: A case study in lake Qinghai, China," in *Proc. IEEE Int. Geosci. Remote Sens. Symp.*, 2020, pp. 6109–6112.

[19] D. R. Doelling, D. Morstad, B. R. Scarino, R. Bhatt, and A. Gopalan, "The characterization of deep convective clouds as an invariant calibration target and as a visible calibration technique," *IEEE Trans. Geosci. Remote Sens.*, vol. 51, no. 3, pp. 1147–1159, Mar. 2013.

[20] B. Zhang, X. Hu, W. Zhou, L. Wang, L. Chen, and P. Zhang, "Radiometric response evaluation of FY-3D/MERSI-II reflective solar bands based on deep convective cloud (in Chinese)," *Acta Optica Sinica*, vol. 43, no. 18, 2023, Art. no. 1828003.

[21] F. Wang, C. Liu, B. Yao, X. Hu, P. Zhang, and B.-J. Sohn, "Cloud-target calibration for Fengyun-3D MERSI-II solar reflectance bands: Model development and instrument stability," *IEEE Trans. Geosci. Remote Sens.*, vol. 61, 2023, Art. no. 5401313.

[22] L. Wang, X. Hu, Z. Zheng, and L. Chen, "Radiometric calibration tracking detection for FY-3A/MERSI by joint use of snow targets in South and North Poles (in Chinese)," *Acta Optica Sinica*, vol. 38, no. 2, 2018, Art. no. 0212003.

[23] C. Cao et al., "Establishing the antarctic dome c. community reference standard site towards consistent measurements from Earth observation satellites," *Can. J. Remote Sens.*, vol. 36, no. 5, pp. 498–513, 2010.

[24] X. Xiong, A. Wu, and B. N. Wenny, "Using dome C. for moderate resolution imaging spectroradiometer calibration stability and consistency," *J. Appl. Remote Sens.*, vol. 3, no. 1, 2009, Art. no. 033520.

[25] L. Mei, V. Rozanov, Z. Jiao, and J. P. Burrows, "A new snow bidirectional reflectance distribution function model in spectral regions from UV to SWIR: Model development and application to ground-based, aircraft and satellite observations," *ISPRS J. Photogrammetry Remote Sens.*, vol. 188, pp. 269–285, 2022.

[26] L. Mei, V. Rozanov, A. Rozanov, and J. P. Burrows, "SCIATRAN software package (V4. 6): Update and further development of aerosol, clouds, surface reflectance databases and models," *Geoscientific Model Develop.*, vol. 16, no. 5, pp. 1511–1536, 2023.

[27] S. G. Warren, R. E. Brandt, and P. O'Rawe Hinton, "Effect of surface roughness on bidirectional reflectance of antarctic snow," *J. Geophysical Res.: Planets*, vol. 103, no. E11, pp. 25789–25807, 1998.

[28] R. Pirazzini, "Surface albedo measurements over Antarctic sites in summer," *J. Geophysical Res.: Atmospheres*, vol. 109, no. D20, 2004, Art. no. 064001.

[29] V. Walden, W. Roth, R. Stone, and B. Halter, "Radiometric validation of the atmospheric infrared sounder over the Antarctic plateau," *J. Geophysical Res.: Atmospheres*, vol. 111, no. D9, 2006.

[30] T. Sadibekova et al., "On the atmosphere for astronomers above Dome C, Antarctica," *Antarctic Sci.*, vol. 18, no. 3, pp. 437–444, 2006.

[31] M. S. Town, V. P. Walden, and S. G. Warren, "Spectral and broadband longwave downwelling radiative fluxes, cloud radiative forcing, and fractional cloud cover over the South Pole," *J. Climate*, vol. 18, no. 20, pp. 4235–4252, 2005.

[32] B. N. Wenny and X. Xiong, "Using a cold Earth surface target to characterize long-term stability of the MODIS thermal emissive bands," *IEEE Geosci. Remote Sens. Lett.*, vol. 5, no. 2, pp. 162–165, Apr. 2008.

[33] S. Uprety and C. Cao, "Using the Dome C. site to characterize AVHRR near-infrared channel for consistent radiometric calibration," in *Proc. Earth Observ. Syst. XVI*, vol. 8153, 2011, pp. 631–639.

[34] X. Xiong, A. Shrestha, and B. Wenny, "Assessments of MODIS thermal emissive bands on-orbit calibration performance using Dome C. observations," in *Proc. Algorithms, Technol., Appl. Multispectral Hyperspectral Imagery XXV*, vol. 10986, 2019, pp. 25–35.

[35] X. Zeng, X. Shao, S. Qiu, L. Ma, C. Gao, and C. Li, "Stability monitoring of the VIIRS day/night band over Dome C. with a lunar irradiance model and BRDF correction," *Remote Sens.*, vol. 10, no. 2, pp. 189–214, 2018.

[36] J. Li et al., "Assessment of BRDF impact on VIIRS DNB from observed top-of-atmosphere reflectance over Dome C. in nighttime," *Remote Sens.*, vol. 13, no. 2, pp. 301–328, 2021.

[37] W. Kim, C. Cao, and S. Liang, "Assessment of radiometric degradation of FY-3A MERSI reflective solar bands using TOA reflectance of pseudo-variant calibration sites," *IEEE Geosci. Remote Sens. Lett.*, vol. 11, no. 4, pp. 793–797, Apr. 2014.

[38] N. Loeb, "In-flight calibration of NOAA AVHRR visible and near-IR bands over Greenland and Antarctica," *Int. J. Remote Sens.*, vol. 18, no. 3, pp. 477–490, 1997.

[39] L. Mei, V. Rozanov, E. Jäkel, X. Cheng, M. Vountas, and J. P. Burrows, "The retrieval of snow properties from SLSTR Sentinel-3–Part 2: Results and validation," *Cryosphere*, vol. 15, no. 6, pp. 2781–2802, 2021.

[40] A. Marks, C. Fragiacomo, A. MacArthur, G. Zibordi, N. Fox, and M. D. King, "Characterisation of the HDRF (as a proxy for BRDF) of snow surfaces at Dome C., Antarctica, for the inter-calibration and inter-comparison of satellite optical data," *Remote Sens. Environ.*, vol. 158, pp. 407–416, 2015.

[41] A. Wu, X. Xiong, and C. Cao, "Using BRDF derived from MODIS observations over Dome C. to characterize calibration stability and consistency of POS sensors," in *Proc. Atmospheric Environ. Remote Sens. Data Process. Utilization V: Readiness GEOSS III*, vol. 7456, 2009, pp. 37–48.

[42] A. Ding et al., "An assessment of the performance of two snow kernels in characterizing snow scattering properties," *Int. J. Remote Sens.*, vol. 40, no. 16, pp. 6315–6335, 2019.

[43] L. Chen, X. Hu, N. Xu, and P. Zhang, "The application of deep convective clouds in the calibration and response monitoring of the reflective solar bands of FY-3 A/MERSI (medium resolution spectral imager)," *Remote Sens.*, vol. 5, no. 12, pp. 6958–6975, 2013.

[44] L. Sun et al., "On-orbit response variation analysis of FY-3 MERSI reflective solar bands based on Dunhuang site calibration (in Chinese)," *Spectrosc. Spectral Anal.*, vol. 32, no. 7, pp. 1869–1877, 2012.

[45] R. Bhatt et al., "Response versus scan-sngle assessment of MODIS reflective solar bands in collection 6.1 calibration," *IEEE Trans. Geosci. Remote Sens.*, vol. 58, no. 4, pp. 2276–2289, Apr. 2020.

Zicheng Yin was born in Ganzhou, China, in 2000. He received the B.E. degree in geographic information science from the College of Oceanography and Space Information, China University of Petroleum, Qingdao, China, in 2022. He is currently working toward the master's degree in resources environment with the School of Geospatial Engineering and Science, Sun Yat-Sen University, Zhuhai, China.

His research interests include polar remote sensing, and radiometric and geometric accuracy validation of FY satellite.

Teng Li was born in Xuzhou, China. He received the B.Sc. degree in geographic science from Wuhan University, Wuhan, China, in 2015, and the Ph.D. degree in global environmental change from Beijing Normal University, Beijing, China, in 2021.

He is currently an Assistant Professor with the School of Geospatial Engineering and Science, Sun Yat-Sen University, Zhuhai, China. His research interests include image processing, glacial dynamics, ice sheet mass balance, and UAV operation.

Linlu Mei received the Ph.D. degree in atmospheric remote sensing under the joint doctoral program between the Institute of Remote Sensing and Digital Earth, Chinese Academy of Sciences, Beijing, China, and the University of Bremen, Bremen, Germany, in 2013.

He was a Senior Research Scientist with the Institute of Environmental Physics, University of Bremen. He is currently a Professor with the International Research Center of Big Data for Sustainable Development Goals and Key Laboratory of Digital Earth Science, Aerospace Information Research Institute, Chinese Academy of Sciences. He is the Principal Investigator of the extensible Bremen aerosol/cloud and surface parameters retrieval algorithm, which is providing global aerosol, cloud, and surface data products for the medium resolution imaging spectrometer and ocean land color instrument instruments. He is also the PI of the fast radiative transfer model fast and accurate semianalytical model of atmosphere-surface reflectance and responsible for the aerosol, cloud, and surface parts in the radiative transfer software package SCIATRAN. His research topics include radiative transfer theory, cryosphere, remote sensing of aerosol, cloud and surface properties, and long-term data creation and applications.

Xiao Cheng was born in Nanjing, China, in 1976. He received the B.E. and M.tech. degrees in engineering survey from the Wuhan Technical University of Surveying and Mapping, Wuhan, China, in 1998 and 2001, respectively, and the Ph.D. degree in cartography and geographical information system from the Graduate School of Chinese Academy of Social Sciences, Beijing, China, in 2004.

In 2004, he joined the Institute of Remote Sensing Applications, Chinese Academy of Sciences, as an Assistant Researcher, and became an Associate Researcher, in 2008. In 2009, he moved to Beijing Normal University and served as the Associate Dean with the College of Global Change and Earth System Science (GCESS), where he became a Professor. In 2016, he became the Dean of GCESS. In 2019, he joined Sun Yat-Sen University, Guangzhou, China, where he initiated the School of Geospatial Engineering and Science and acted as the Dean. He has authored or coauthored more than 100 peer-reviewed journal papers, including *Proceedings of the National Academy of Sciences of the United States of America*, *Remote Sensing of Environment*, and other top international geoscience journals. His research interests include polar remote sensing technology and climate change in polar regions.

Dr. Cheng was a recipient of the Award for advanced individual of China's polar exploration in 2017.
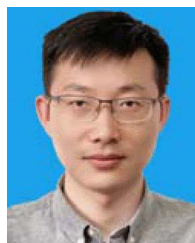
Lei Zheng received the Ph.D. degree in photogrammetry and remote sensing from Wuhan University, Wuhan, China, in 2019.

He is currently an Associate Professor with Sun Yat-Sen University, Guangzhou, China. He has authored or coauthored about 20 publications in refereed journals. His research interests include remote sensing of snow and ice, snow/permafrost/river thermal model, snow microwave emission/backscatter model, with a focus on the melting processes and climate variability in the cryosphere.

Qi Liang received the B.S. degree in information and computing science from the Harbin Institute of Technology, Harbin, China, in 2010, and the M.S. and Ph.D. degrees in photogrammetry and remote sensing from Wuhan University, Wuhan, China, in 2014 and 2019, respectively.

He is currently an Associate Professor with the School of Geospatial Engineering and Science, Sun Yat-sen University, Guangzhou, China. His research interests include using satellite data to monitor glacier changes in Antarctica and Greenland and understand its response to climate change.

Xinqing Li received the M.S. degree in photogrammetry and remote sensing from the Shandong University of Science and Technology, Qingdao, China, in 2015, and the Ph.D. degree in global environment changes from Beijing Normal University, Beijing, China, in 2020.

He is currently an Engineer on remote sensing with the Southern Marine Science and Engineering Guangdong Laboratory, Zhuhai, China. His research interests include the theory and technologies of sea ice remote sensing and numerical modeling.